

pubs.acs.org/JACS Article

Cell-Free Nonequilibrium Assembly for Hierarchical Protein/Peptide Nanopillars

Jiaqi Guo, Ayisha Zia, Qianfeng Qiu, Michael Norton, Kangqiang Qiu, Junichi Usuba, Zhiyu Liu, Meihui Yi, Shane T. Rich-New, Michael Hagan, Seth Fraden, Grace D. Han, Jiajie Diao, Fengbin Wang,* and Bing Xu*



Cite This: J. Am. Chem. Soc. 2024, 146, 26102-26112



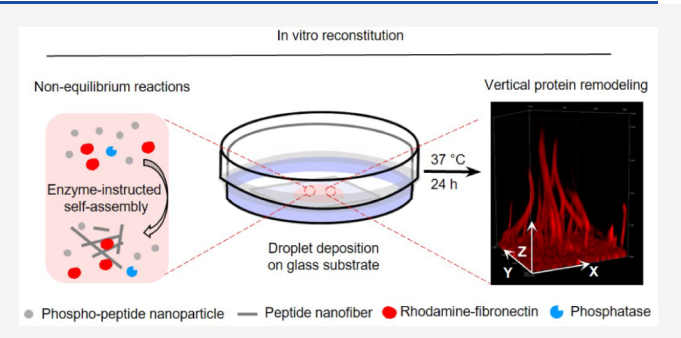
ACCESS

Metrics & More

Article Recommendations

Supporting Information

ABSTRACT: Cells contain intricate protein nanostructures, but replicating them outside of cells presents challenges. One such example is the vertical fibronectin pillars observed in embryos. Here, we demonstrate the creation of cell-free vertical fibronectin pillar mimics using nonequilibrium self-assembly. Our approach utilizes enzyme-responsive phosphopeptides that assemble into nanotubes. Enzyme action triggers shape changes in peptide assemblies, driving the vertical growth of protein nanopillars into bundles. These bundles, with peptide nanotubes serving as a template to remodel fibronectin, can then recruit collagen, which forms aggregates or bundles depending on their types. Nanopillar



formation relies on enzyme-catalyzed nonequilibrium self-assembly and is governed by the concentrations of enzyme, protein, peptide, the structure of the peptide, and peptide assembly morphologies. Cryo-EM reveals unexpected nanotube thinning and packing after dephosphorylation, indicating a complex sculpting process during assembly. Our study demonstrates a cell-free method for constructing intricate, multiprotein nanostructures with directionality and composition.

■ INTRODUCTION

Proteins are the fundamental building blocks of life, forming complex, hierarchical nanostructures within cells, such as the ribosome, inflammasome, and microtubule organizing center.3 Recent advancements in cell biology and structural biology reveal the intricate details of these nanostructures,⁴ providing valuable blueprints for mimicry in cell-free systems. Using this approach to generate hierarchical protein nanostructures not only eliminates the complexities and interference from irrelevant cellular components but also offers a promising avenue for understanding and mimicking biological processes. Despite its potential, the cell-free formation of hierarchical protein nanostructures remains challenging. Current approaches for generating protein superstructure mainly focus on self-assembly at thermodynamic equilibrium, which limits the ability to mimic the structural and dynamic continuum⁶ observed in natural protein systems. In cells, biological processes operate far from equilibrium. For example, self-organization of actin filaments and microtubules arises from nonequilibrium interactions among subunits, involving constant exchange of energy and matter from the environment via enzymatic reactions. Therefore, exploring nonequilibrium self-assembly within cell-free systems is crucial for mimicking natural processes to generate hierarchical protein nanostructures.

While some synthetic materials have replicated aspects of protein assembly, such as energy dissipation or chirality, they often overlook other key features. Mimicking the specific directionality seen in natural systems, like the flagellar secretion system extended from the cell surface, presents a significant challenge. Similarly, the dynamic aspects of the extracellular matrix (ECM) have been largely overlooked. Traditionally, ECM was viewed as a random mesh of protein fibers with emphasis on its adhesive properties. Recent studies of fibronectin, a key ECM component, reveal its ability to form directionally structured architectures. Mechanical forces influence fibronectin's orientation and induce fibrillogenesis, as demonstrated in Vogel's work. 10 Research by Sato et al. highlights the dynamic role of fibronectin, revealing unexpected micrometer-long fibronectin pillars. These pillars, formed by pulsatile blood flow, serve to connect embryonic layers. 11 This new understanding of dynamic ECM architectures has opened doors for fundamental research and the

Received: May 17, 2024 Revised: August 28, 2024 Accepted: August 29, 2024 Published: September 10, 2024





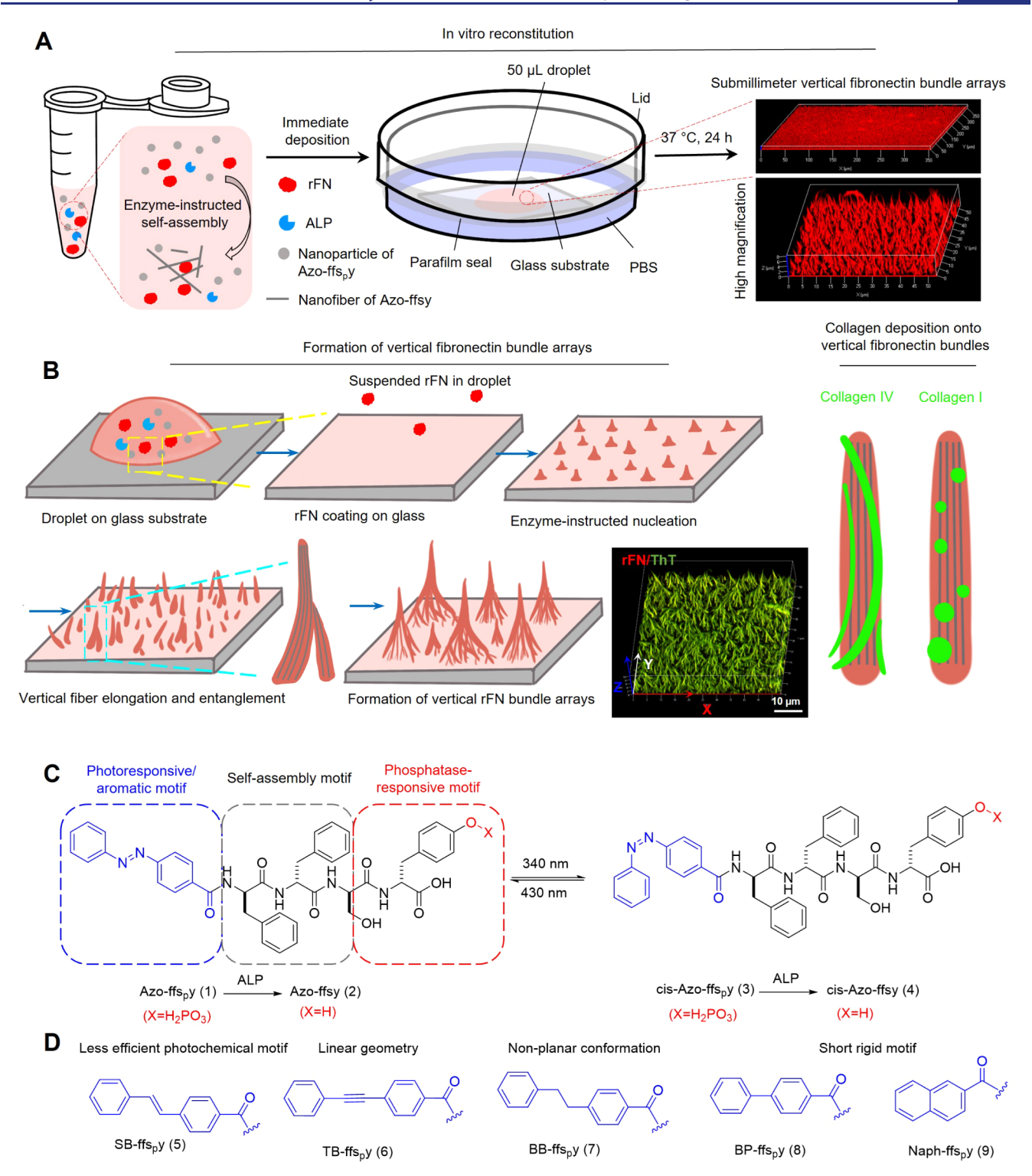


Figure 1. Molecular design of Azo-ffs_py and its analogues. (A) Schematic illustration showing the setup of cell-free generation of submillimeter vertical fibronectin pillar arrays. (B) Schematic illustration showing the formation of vertical fibronectin bundle arrays that remodel collagen I or collagen IV into distinct morphologies. (C) Chemical structures of Azo-ffs_py and its products upon photoisomerization and/or dephosphorylation. (D) Analogues of Azo-ffs_py when substituting the aromatic motifs.

design of biomimetic materials, particularly from the perspective of nonequilibrium self-assembly.

Inspired by the above works, we aimed to mimic the fibronectin pillars¹¹ formed by dynamic mechanical manipulation. While creating pulsatile flow at the cellular level is illuminating, the key is to introduce nonequilibrium self-assembly to the equation. Enzymatic self-assembly, a versatile

form of this process, ¹² can generate cytoskeleton-like architecture in cellular environments, ¹³ as well as enable cell-spheroid formation. ¹⁴ Therefore, it is possible to replicate the generation of local tensional force ¹⁵ by the enzyme-driven morphogenesis of peptide assemblies for making the fibronectin pillars. Here, we report a multiscale self-organization process where enzyme catalysis transforms the

morphologies of peptide assemblies, as a process of nonequilibrium self-assembly. Our approach uses enzymatic reactions to introduce continuous energy input, maintaining the system in a dynamic state. This process generates peptide/ protein pillars consisting of key components of the ECM, such as fibronectin and collagens (Figure 1A). Specifically, alkaline phosphatase (ALP) dephosphorylates an N-terminal azobenzene-capped phosphotetrapeptide (Azo-ffs_ny), transforming the nanoparticles of the phosphopeptides into nanofibers and driving the nucleation of fibronectin on a glass substrate. The emerging nucleation sites initiate vertical growth and entanglement into peptide/protein pillars, which eventually intertwine into vertical bundle arrays about eight micrometers in height. The interaction between fibronectin and collagen type I or IV results in composite pillars visualized under electron microscopy as bundles consisting of protein and peptide fibers. Without the enzymatic reaction, no vertical protein pillars would form. Further investigation shows that the length and diameters of the pillars are determined by the rates and extent of enzymatic reaction, concentrations of starting materials, and surface net charge rather than the equilibrium composition. Photomodulation impacts the enzymatic morphogenesis of the photoresponsive Azo-ffs_ny, subsequently influencing vertical fibronectin remodeling. Cryo-EM structures reveal that the peptides self-assemble into helical nanotubes and suggest an unexpected decrease in diameter (from 50 to 45 Å) upon dephosphorylation. This confirms the conformational change of the peptide molecules by the enzymatic reaction and, along with photomodulation studies, indicates a structural and dynamic continuum⁶ of higher-order peptide assemblies. Studies on Azo-ffs_py analogues suggest a potential role of the distance between N-terminal capping aromatics and diphenylalanine in pillar formation. This work demonstrates a cell-free, nonequilibrium self-assembly approach for mimicking biological self-organization. By engineering molecular structures and enzymatic reactions, we can create hierarchical protein assemblies with directional bias ranging from nano- to microscales. This offers a powerful strategy for creating well-defined protein nanostructures with potential applications in regenerative medicine ¹⁶ and material science.¹⁷ Moreover, this work breaks new ground by utilizing enzymatic reactions to construct peptide/protein pillars, departing from traditional nonequilibrium self-assembly methods that rely on chemical fuels. This enzymatic approach to organizing protein nanostructures unlocks a novel and potentially transformative avenue for the development of advanced materials and functionalities.

■ RESULTS AND DISCUSSION

Cell-Free Setup for Hierarchical Protein Nanopillars. A cell-free experimental setup was used (Figure 1A). A mixture of peptide precursors (e.g., Azo-ffs_py), rhodamine-fibronectin (rFN), and ALP in phosphate buffered saline (PBS) is deposited onto a glass bottom confocal dish, supplemented with a PBS rim for in-dish humidity control. The confocal dish is then sealed with parafilm and incubated at 37 °C (Figure S1). Schematic illustration displays microscale self-organization of fibronectin into vertical pillars (Figure 1B). Monitoring the morphogenesis over time, we observed that fibronectin coating on glass is accompanied by enzyme-instructed dephosphorylation of D-peptide, which drives the nucleation of fibronectin (Figure 3C, vide infra). Subsequently, this process initiates vertical pillar growth and entanglement, leading to a previously

unseen hierarchical protein nanostructure composed of pillars made of proteins and peptides (Figure 3C). The presence of peptide nanofibers within the pillars is supported by positive thioflavin T (ThT) staining (Figures 1B and S26). These peptide/protein pillars eventually intertwine to form vertical bundle arrays. The peptide/protein pillars act as templates, which effectively guide type I or IV collagen into spherical or bundled morphologies, respectively (Figure 3G).

Design and Synthesis of Precursors for Fibronectin Remodeling. The molecular structure of the D-peptide, depicted in Figure 1C, includes an azobenzene (Azo) as a photosensitive and aromatic motif, and D-phenylalanine-Dphenylalanine (ff)¹⁸ to promote self-assembly. A D-serine-Dphosphotyrosine complex is connected to the C-terminus of ff, rendering it responsive to phosphatases. We chose D-peptides because they resist proteolysis, and previous work¹⁴ has shown that D-peptide fibrils can interact with fibronectin. While this work focuses on D-peptides, L-peptide fibrils might also interact with fibronectin in a similar manner. This is because CsgA, a protein known to bind fibronectin, is composed of L-amino acids. This design leads to the key molecule, Azo-ffs_py (1), which in principle undergoes photoisomerization upon UV irradiation to generate cis-Azo-ffs_ny (3). Enzymatic dephosphorylation of 1 or 3 forms Azo-ffsy (2) or cis-Azo-ffsy (4), respectively. To explore the vertical fibronectin remodeling via molecular design, analogues with varied aromatic motifs were synthesized (Figure 1D). For instance, (E)-stilbene (SB) is selected as a less efficient photochemical motif, while diphenylethyne (TB) functions as a linear motif with moderate rotational flexibility. Diphenylethane (BB) is a nonlinear motif with increased rotational flexibility. Additionally, biphenyl (BP) serves as a nonplanar rigid motif, featuring a dihedral angle between two benzene rings, and naphthalene (Naph) acts as a planar motif, with the fused Naph being more rigid and shorter in length. This design creates SB-ffs_py (5), TB-ffs_py (6), BB-ffs_py (7), BP-ffs_py (8), and Naph-ffs_py (9). We synthesized these compounds using solid-phase peptide synthesis (SPPS) and confirmed their identity by liquid chromatography-mass spectrometry (LC-MS) (Scheme S1, Figures S2-S7).

Photoisomerization and Enzymatic Self-Assembly of Azo-ffs_py. Photoirradiation and phosphatase incubation were conducted to characterize the dual responsiveness of Azo-ffs_py. The absorbance spectra obtained under various wavelengths provide insight into the photochemistry of the azobenzene motif. UV irradiation at 340 and 365 nm facilitated the formation of *cis*-Azo-ffs_py, resulting in increased absorbance at 250 nm. In contrast, visible light at 430 and 470 nm maintained the *trans* conformation with a characteristic peak around 320 nm (Figure 2A). The absorbance at 323 nm was plotted against the irradiation time to determine the minimal time required to reach the photostationary state (Figure 2B). Based on these results, irradiation at 340 nm for 60 min was used for *trans* to *cis* transition and 430 nm for 10 min for *cis* to *trans* isomerization.

High-performance liquid chromatography (HPLC) proved effective in determining the *cis/trans* composition in Azo-ffs_py (Figure S8). Therefore, we calculated the *cis/trans* ratios under various conditions based on peak areas (Figure 2C). Ambient Azo-ffs_py consists of 14% *cis* isomer and 86% *trans* isomer. Irradiation at 340 nm shifts the composition to 92% *cis* and 8% *trans*, while 430 nm irradiation reverses it to 23% *cis* and 77% *trans*. The half-life of *cis*-Azo-ffs_py is 20 days at 25 °C and 19.2

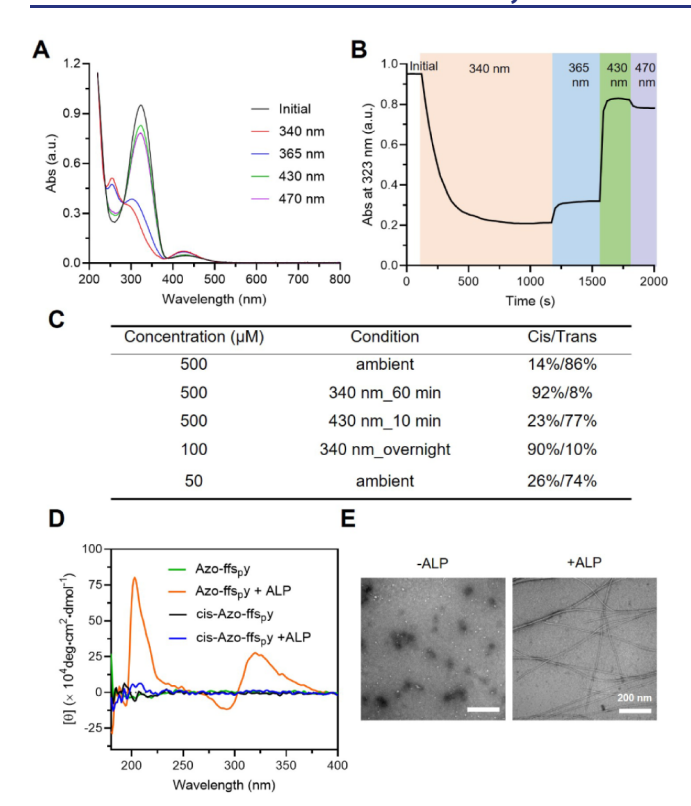


Figure 2. Dual-responsive short peptides self-assemble into nanofibers. (A) UV absorbance of Azo-ffs_py under different irradiation wavelengths. (B) Absorbance at 323 nm ($A_{323 \text{ nm}}$) under different irradiation wavelengths over time. (C) Cis/Trans ratios of Azo-ffs_py after different treatments. (D) CD spectra of Azo-ffs_py or cis-Azo-ffs_py in the presence or absence of ALP for 24 h. (E) TEM images of Azo-ffs_py in the presence or absence of ALP for 24 h. Cis-Azo-ffs_py is prepared by 340 nm irradiation for 60 min. [Azo-ffs_py] = [cis-Azo-ffs_py] = 50 μ M, [ALP] = 0.1 U/mL, unless otherwise specified.

days at 37 °C, indicating that Azo-ffs_py undergoes negligible conformational changes during a 24-h incubation (Figure S9). However, the dephosphorylated product, Azo-ffsy, undergoes incomplete photoisomerization and quickly reverts to the *trans* conformation under 430 nm irradiation (Figure S10). Determining the thermostability of *cis*-Azo-ffsy proved challenging as elevated temperatures alter its initial absorbance, probably due to the temperature-sensitive noncovalent self-assembly (Figure S11).

Furthermore, incubating Azo-ffs_py with ALP results in nearcomplete dephosphorylation in 4 h, producing both cis and trans isomers of the products (Figure S12). The partial overlap between the peaks of trans-Azo-ffs_py and cis-Azo-ffsy (Figure S12) hinders the confirmation that trans-Azo-ffs_py is dephosphorylated faster than cis-Azo-ffs_ny. This enzymatic dephosphorylation decreases the critical micelle concentration (CMCs) (Figure S13), thereby initiating self-assembly to form β sheet-rich structures, evidenced by the acute signal around 200 nm in the circular dichroism (CD) spectra (Figure 2D). Induced-CD signals (250–400 nm) originated from the helical arrangements of the azobenzene motif (Figure 5, vide infra). Cis-Azo-ffsy, however, failed to form secondary structures. Transmission electron microscopy (TEM) images display a morphological transformation of ambient Azo-ffs_py (predominately trans) from nanoparticles to nanofibers upon ALP incubation (Figure 2E), whereas the 340 nm photoswitched Azo-ffs_py (predominantly *cis*) retains a particle morphology

with additional sparse nanofibers, possibly due to the presence of a trans isomer at the photostationary state (Figure S14). These observations are consistent with the CD spectra, where no significant β -sheet formation is observed in *cis*-Azo-ffs_py after dephosphorylation. The lack of ordered secondary structures in cis-Azo-ffs, y likely results from the steric hindrance and nonplanar structure caused by the twisted azobenzene moiety, preventing the extensive $\pi - \pi$ stacking necessary for the formation of higher-ordered nanostructures. While postassembly photoisomerization is inefficient and does not alter Azo-ffsy's fibrillar morphology (Figure S15), photomodulating the cis/trans ratio of Azo-ffspy controls the morphologies of peptide assemblies in an orthogonal fashion to enzymatic reactions. This photomodulation provides an additional handle to tailor the vertical protein pillars (Figure 4I,I, vide infra) and for understanding the critical role of peptides' morphogenesis.

Enzymatic Transformation Induces Vertical Fibronectin Bundles. Depositing a mixture of Azo-ffs_ny, ALP, and rFN results in the growth of vertical fibronectin-containing pillars on the glass substrate (Figure S16), while Azo-ffs, y or ALP alone retains the globular morphology of rFN (Figure S17). Structured illumination microscopy (SIM) reveals these vertical fibers, around 8 μ m in length, form flexible, entangled bundles with tapering tips (Figure 3A,B). This hierarchical assembly, beginning from fiber convergence within 2 μ m of growth, is suggested to result from elastocapillary assembly, where the interfacial tension of a wetting fluid draws the fibers together (Supporting Discussions in the Supporting Information). This mechanism differs from Marangoni flow, which creates radial protein alignments, 19 and diverges from the vertical alignment seen in supramolecular polymers, which is characterized by liquid-liquid phase separation (Figure S18).20

Time-series imaging of fixed samples reveals the rapid formation of vertical bundles within 60 min (Figure 3C). Fibronectin establishes a homogeneous coating on glass within 6 min, initiating protrusions on the coating between 12 and 18 min, representing the nucleation sites for fibers. Fiber elongation mainly occurs from 30 to 60 min and meanwhile initiates the hierarchical assembly of fibers into bundles. In situ real-time imaging was suboptimal because repeated imaging of the same area caused photobleaching, displaying halted bundle growth from 4 to 8 μm (Figure S19). In contrast, the nearby region displays normal vertical bundles of 8 μm (Figure S20).

Given the diverse interactions of native fibronectin with various ECM components, we sought to investigate the remodeling effects of established bundles on collagen, which is a major ECM protein. Azo-ffs_ny preserves the globular structures of Collagen I and IV with no vertical arrangements (Figure S21). However, vertical fibronectin bundles successfully remodel these collagens with good colocalization (Figure 3D,E). The vertical bundles exhibit a more efficient remodeling of collagen compared with the bottom layer (Figures S22 and S23). This observation suggests distinct conformations: the bottom layer mainly consists of globular fibronectin with most interaction sites folded inside, whereas the vertical bundles are enriched in fibrillar fibronectin that actively engages in protein interactions. Cross sections of the composite pillars show partial colocalization between rFN and Collagen I/IV-FAM (Figure S24). Notably, the fluorescence intensity of the two channels displays an offset, indicating that the peptide-

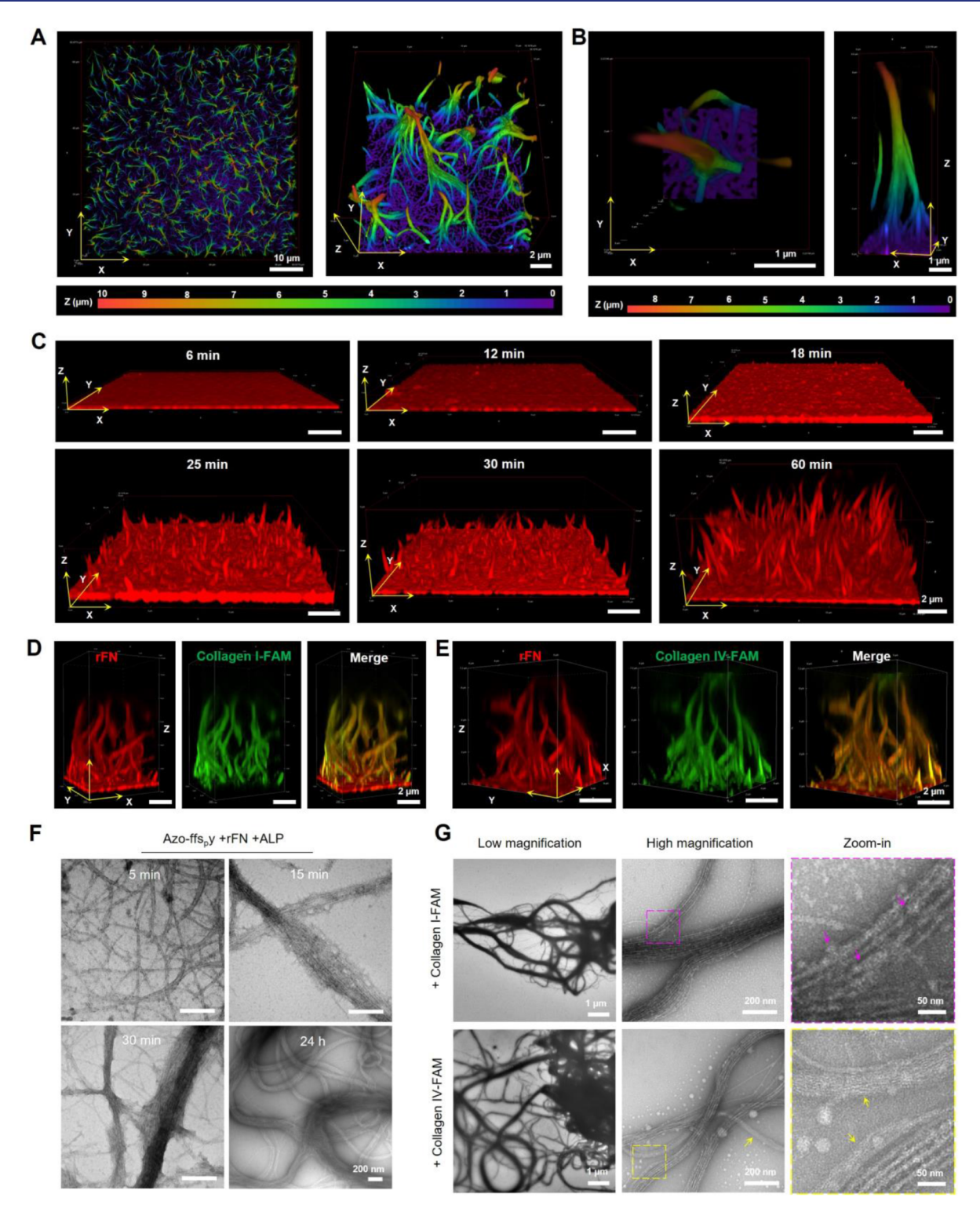


Figure 3. Enzymatic self-assembly drives the growth of vertical fibronectin fiber arrays. (A) Low magnification and (B) high magnification 3D rendering SIM images of Azo-ffs_py incubated with rFN in the presence of ALP for 24 h. (C) 3D rendering SIM images of Azo-ffs_py incubated with rFN in the presence of ALP for designated period (6–60 min) and fixed with paraformaldehyde. 3D rendering SIM images of Azo-ffs_py incubated with rFN in the presence of ALP for 24 h and then supplemented with (D) Collagen I-FAM, or (E) Collagen IV-FAM for another 24 h. (F) TEM images of Azo-ffs_py incubated with rFN in the presence of ALP for designated period. (G) TEM images of the sample in (D) and (E). Magenta arrows point to collagen I-FAM aggregates in bundles. Yellow arrows point to collagen IV-FAM bundles next to the peptide nanofibers or bundles. [Azo-ffs_py] = 50 μ M, [rFN] = [collagen I-FAM] = [collagen IV-FAM] = 50 μ g/mL, [ALP] = 0.1 U/mL, incubation temperature is 37 °C.

fibronectin pillars serve as a template guiding the deposition of collagen onto the existing structures.

TEM images display the morphological transformation from small, single-layer bundles (5-15 min) to wider bundles (30 min)

min) and eventually to densely packed, entangled bundles (24 h) (Figure 3F). These close-packed bundles display fibronectin aggregates between Azo-ffsy nanofibers upon serial dilution (Figure \$25).

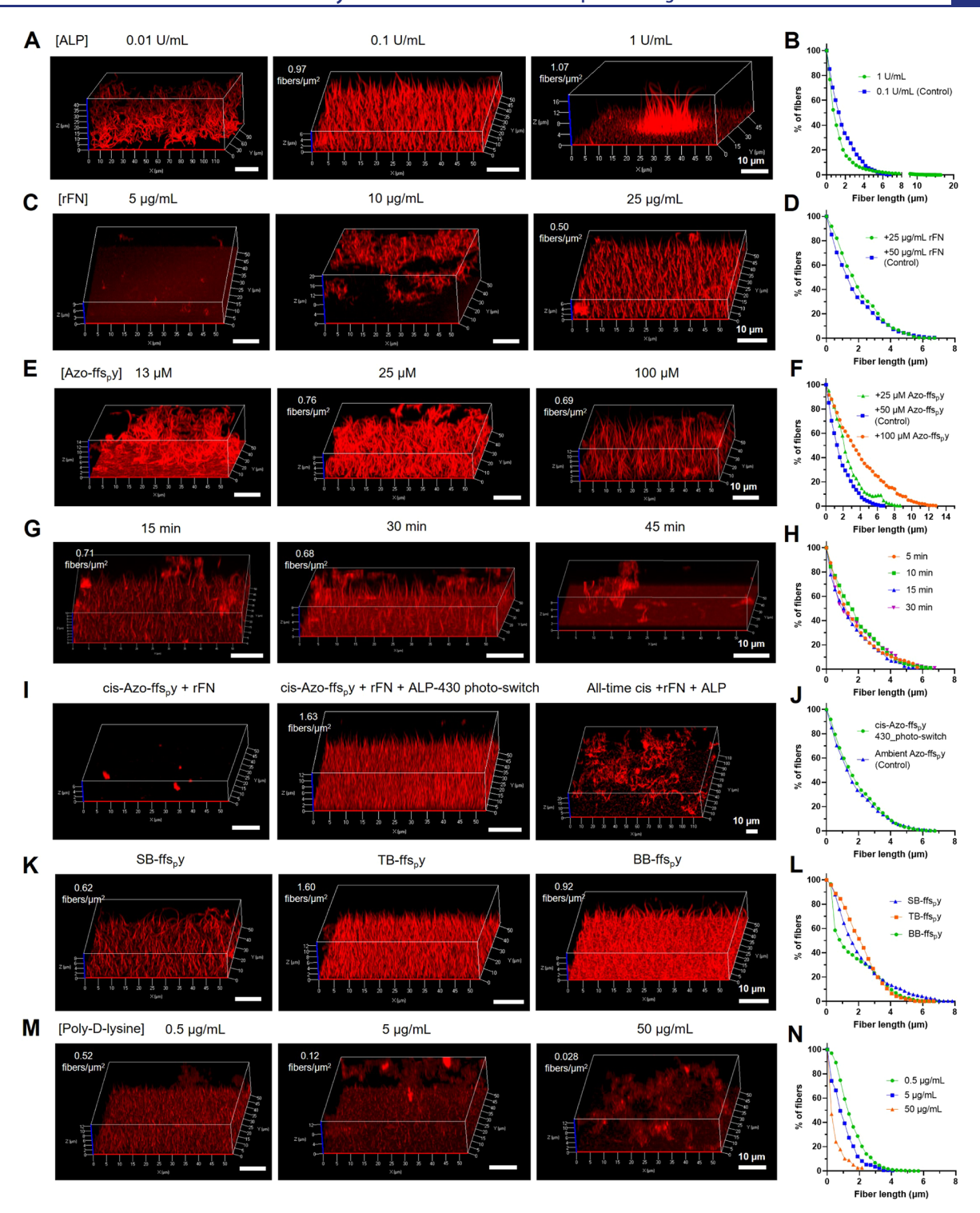


Figure 4. Crucial role of enzyme-instructed assembly for vertical fibronectin fiber array formation. (A) 3D confocal images and (B) vertical fiber quantification of Azo-ffs_py with rFN in the presence of ALP (0.01–1 U/mL). The sample with 0.1 U/mL ALP addition in (A) is considered control in the following figures. (C) 3D confocal images and (D) vertical fiber quantification of Azo-ffs_py, rFN (5–25 μ g/mL), and ALP. (E) 3D confocal images and (F) vertical fiber quantification of Azo-ffs_py (13–100 μ M), rFN, and ALP. (G) 3D confocal images and (H) vertical fiber quantification of Azo-ffs_py in the treatment of ALP for a designated period (15–45 min) and then supplemented with rFN for 3 h. (I) 3D confocal images and (J) vertical fiber quantification of *cis*-Azo-ffs_py and rFN; *cis*-Azo-ffs_py, rFN, and ALP for 1 h and then 430 nm irradiation for 10 min; and all-time *cis*-Azo-ffs_py, rFN, and ALP. (K) 3D confocal images and (L) vertical fiber quantification of analogues with rFN in the presence of ALP. (M) 3D confocal images and (N) vertical fiber quantification of Azo-ffs_py, rFN, and ALP deposited onto a poly-D-lysine (0.5–50 μ g/mL) coated confocal dish. [Azo-ffs_py] = [*cis*-Azo-ffs_py] = [SB-ffs_py] = [BB-ffs_py] = 50 μ M, [rFN] = 50 μ g/mL, [ALP] = 0.1 U/mL, incubation temperature is 37 °C, and incubation time is 24 h unless otherwise specified.

The vertical pillar formation is sensitive to the modification of the peptide molecule, as replacing azobenzene with 4chloro-7-nitrobenzofurazan, which serves as both an aromatic motif and a fluorescent probe, fails to induce vertical pillars. 14

Therefore, we conducted staining on established pillars to visualize the peptide nanofibers. ThT staining reveals the β -sheet-rich structures within the pillars, providing an approach to visualize peptide nanofiber distribution. The colocalization between ThT and rFN indicates the presence of both peptide and protein within the pillars (Figure S26).

To determine the nanoscale morphology of the remodeled collagen, we took TEM images of the bundles prepared in Figure 3D,E. Type I collagen remains as globular aggregates on and between the established bundles, whereas type IV collagen assembles into bundles adjacent to existing ones (Figures 3G and \$27).

In addition to in vitro remodeling of ECM protein, Azo-ffs $_p$ y also functions in a cellular environment, manipulating cell aggregation to generate spheroids with photo responsiveness (Figure S28). The fixed vertical protein pillars are cell-compatible, displaying uncompromised vertical arrangements upon cell attachment (Figure S29).

Tailoring Vertical Fibronectin Bundles. To elucidate the contributions of individual components to the formation of vertical bundles, we varied the parameters, including starting material concentration, extent of reaction, peptide conformation, surface net charge, and temperature. In addition to confocal 3D visualization, a quantification assay was employed to assess vertical fibers (Scheme S2).

Figure 4A shows the ALP-dependent morphological changes in remodeled fibronectin. ALP at 0.1 U/mL results in uniform vertical bundles, whereas reducing the ALP concentration abolishes this vertical arrangement, leading to the formation of an interwoven fibronectin network. Increasing the concentration to 1 U/mL induces heterogeneity, forming long bundles up to 16 μ m (Figure 4B). Substituting ALP with prostatic acid phosphatase (PAP) maintains bundle formation, indicating the versatility of this vertical remodeling process and its potential applicability with a range of enzymes (Figure S30). We hypothesized that the enzyme-instructed formation of β -sheet-rich nanofibers creates dynamic forces under nonequilibrium conditions, potentially facilitating fibronectin's fibrillogenesis from a soluble state to an insoluble fibril state, thereby promoting nucleation.

The vertical fiber formation depends on a minimum fibronectin concentration, as insufficient levels do not produce vertical bundles on the glass substrate (10 μ g/mL) and may prevent any fibrillar structure development (5 μ g/mL; Figure 4C). Reducing the fibronectin concentration to 25 μ g/mL generates bundles with a similar length distribution, however with approximately half the fiber density (Figure 4D).

Moreover, the peptide concentrations affect the morphology of the remodeled fibronectin. At 100 μ M, Azo-ffs_py guides the formation of bundles of 13 μ m, albeit with decreased fiber density. In contrast, 25 μ M Azo-ffspy induces wavy vertical fibronectin bundles with lengths comparable to those of the control (Figure 4E,F). This represents an intermediate stage between vertical bundles and a random fibrous network. Further dilution to 13 μ M Azo-ffs_py fails to instruct the vertical alignment of fibers, suggesting that D-peptide nanofibers increase the stiffness of the peptide—protein assemblies to promote their vertical alignment.

Azo-ffsy $(6.3-25 \mu M)$, when used below its CMC, induces random networks of fibrous rFN (Figure S31). With further dilution to 3.1 μ M, the fibrillogenic capability of Azo-ffsy decreases, with only a few rFN fibrils observed. We reasoned that rFN facilitates the self-assembly of Azo-ffsy, promoting

aggregation to 3.1 μ M in this context. Since Azo-ffsy is incapable of constructing pillars independently, it is the enzymatic self-assembly process that serves as the driving force behind pillar formation.

These results suggest that supramolecular self-assembly provides the prerequisite for vertical pillar formation. Additionally, the nonequilibrium conditions of ongoing selfassembly are crucial for dictating the directionality, as systems at equilibrium fail to induce vertical pillars. There is a subtle balance among the concentrations of peptide, protein, and enzyme to induce the formation of vertical pillars. We reasoned that this is related to the balance between the nucleation and elongation process. Monitoring the vertical pillar formation for the first 3 h, we observed a gradual increase in fiber density from 1 h to 2.5 h, with a plateau reached at 2.5 h (Figure S32). This indicates that the nucleation process lasts for over 2 h. As for the fiber length, the percentage of fibers of different lengths did not vary significantly between time points, with the elongation process occurring within the first 1.5 h, as the maximum fiber length remained unchanged thereafter. These results indicate a slower nucleation process compared to elongation, which can explain the lower fiber density observed in longer pillars (Figure 4). Systems with higher peptide concentrations take a longer time to reach equilibrium and have more "fuel" to drive the vertical growth of pillars. As a result, fibronectin is primarily consumed for elongation, rather than nucleation. The length of the initial fiber affects the early structure but is unlikely to determine the final height of the vertical structures. These structures continue to grow taller due to chemical reactions in an unstable environment. More building blocks lead to taller final structures because there's more material to work with and it takes longer for the system to stabilize.

To vary the extent of enzymatic reaction, we incubated Azoffs_ny with ALP for different durations and then supplemented with rFN. Results show that the vertical bundle arrays disappear when rFN addition is delayed for 45 min or more (Figures 4G,H and S33). These findings imply that vertical remodeling requires simultaneous interaction among the peptide, protein, and enzyme components from the onset, potentially to facilitate the initial heterogeneous nucleation, which is crucial for further elongation. The critical role of early stage coassembly is further demonstrated by the fact that preassembled enzymatic nanofibers, as well as precoated fibronectin, failed to generate vertical bundles (Figures S34 and S35). These results highlight the necessity of nonequilibrium self-assembly for the formation of the vertical fibronectin pillars. Photoswitching the ambient Azo-ffs_py into cis majority fails to remodel vertical fibronectin (Figures 4I and \$36). However, if an additional 430 nm photoirradiation is applied to revert to the trans-isomer, the vertical bundles are restored with higher density (Figure 4I,J). This photoswitching approach allows us to explore the impact of accelerated nucleation on overall pillar formation.

Substituting azobenzene for SB, which predominantly adopts a pure *trans* conformation in its LC–MS spectrum, preserves the vertical alignment of fibronectin (Figure 4K). This finding implies that the vertical fibronectin structure is not dependent on the *cis* conformation or the presence of nitrogen atoms in the aromatic motif. Similarly, substitution of azobenzene with TB maintains this morphology, demonstrating insensitivity to the linear aromatic motif geometry. BB-ffs_py also retains the vertical fibronectin alignment, indicating

minimal planarity requirements for the N-terminal capping motif. The vertical bundles remodeled by the aforementioned analogues measure 6-8 μ m in height and exhibit different fibrillar densities and distinct morphology at the bottom slice (Figures 4K,L and S37). However, BP- and Naph-capped peptides do not lead to vertical bundles. BP-ffs_py leads to random fibronectin networks, and Naph-ffs_py fails to generate fibrillar structures, possibly due to the aggregate morphology of dephosphorylated Naph-ffsy (Figure S38). Molecular optimization of D-peptides reveals distinctions among aromatic analogues, with biphenyl and naphthalene motifs being notably shorter (Figure S39), which might influence the interactions between protein-peptide assemblies and the glass substrate. Although there is a correlation between the size of the aromatic motif and the fibrillar morphology of dephosphorylated D-peptides, the fact that the aromatic motifs are embedded in the fiber cores (Figure 5, vide infra) suggests

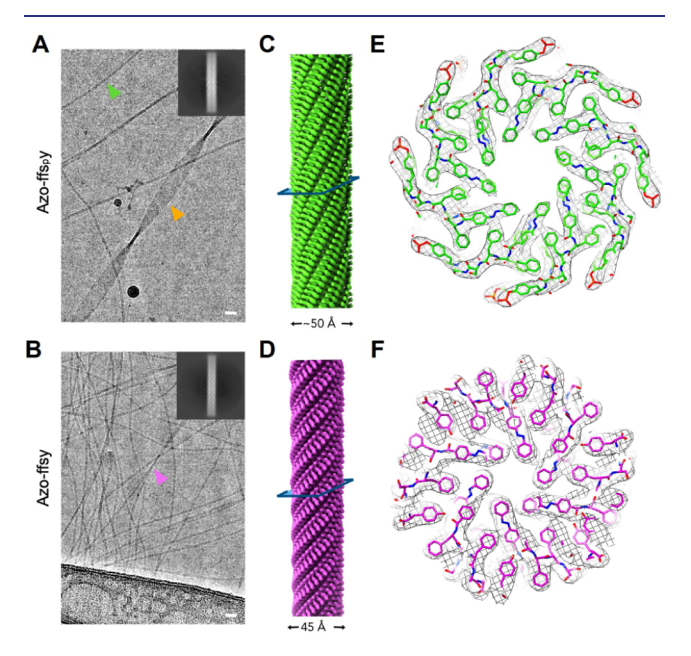


Figure 5. Cryo-EM of Azo-ffs_py (pH 4) and Azo-ffsy nanofibers. Representative cryo-EM micrographs and 2D average of (A) 20 μ M Azo-ffs_py (pH 4) and (B) 20 μ M Azo-ffsy nanofibers. Filaments with different morphologies were labeled with colored arrows in the Azo-ffs_py (pH 4) sample. Scale bars are 20 nm. 3D helical reconstructions of (C) Azo-ffs_py (pH 4) and (D) Azo-ffsy nanofibers. The cross-sectional view of (E) Azo-ffs_py (pH 4) and (F) Azo-ffsy nanofibers, with atomic models built into the cryo-EM maps.

limited direct interaction with external proteins. Besides, variations in CMC before and after dephosphorylation (Figure S13), as well as potential differences in dephosphorylation and fiber formation kinetics, likely play a more important role in the out-of-equilibrium process.

While the detailed molecular interaction between the Dpeptide and fibronectin remains unclear, it is possible that fibronectin, containing a positively charged domain, interacts with the negatively charged Azo-ffs_py aggregates through electrostatic interactions. This interaction could initiate fibrillogenesis by EISA. Once peptide fibrils form, they might also bind rFN due to their structural similarity to CsgA, which is known to bind fibronectin. Therefore, to modify the net charge of the surface, poly-D-lysine at various concentrations was used for glass coating to examine the effects of charge on

morphogenesis. Charge undermines vertical bundle formation, leading to both decreased bundle length and fiber density as poly-D-lysine concentration increases (Figure 4M,N). As demonstrated by Liamas et al., the adsorption of fibronectin fragments on amine surfaces is rapid and site-specific.²¹ The protein quickly rotates and aligns its dipole moment, resulting in the negatively charged side anchoring to the surface. In contrast, adsorption on uncharged surfaces is slower and nonspecific, driven by Brownian motion until the right residue anchors. The electrostatic interactions between the poly-D-lysine coated surface and the protein/peptide would likely override fibronectin—peptide interactions, therefore altering fibronectin's orientation and conformation, eventually leading to the random aggregation observed in Figure 4M.

Inverted incubation of a hanging drop on glass retains the vertical alignment, suggesting that the vertical orientation is driven by intrinsic properties of the system, such as forces generated by enzymatic self-assembly, rather than being influenced by gravity (Figure S40).

Confocal images from different regions of the droplet, including the center, near the edge, and the edge reveal a similar pillar morphology, indicating uniformity throughout the droplet (Figure S41).

Temperature is also critical, with room temperature (22 $^{\circ}$ C) showing elimination of vertical structures, whereas elevated temperatures (42 $^{\circ}$ C) initially show enhanced bundle length but lead to disruption at higher levels (50 $^{\circ}$ C) (Figure S42). We hypothesized that the temperature-dependent nature of fibronectin's conformation, enzymatic dephosphorylation rate, and nanofiber self-assembly collectively contribute to the subtle temperature preference observed.

Enzymatic Remodeling of Peptide Nanofibers. We next wondered how the peptide nanofiber architecture changes upon ALP treatment, which leads to the dephosphorylation of terminal D-tyrosine. To replicate the increased intermolecular stacking during dephosphorylation, we protonated the Cterminus of Azo-ffs_py (pH 4), resulting in a mixture of nanoparticles, sheets, and fibers at 100 μ M (Figure S43). In this way, we aimed to simulate a potential intermediate stage of enzymatic dephosphorylation. Thus, we imaged both Azo-ffs_py (pH 4) and Azo-ffsy (Azo-ffs_py treated with ALP) by using cryo-EM. Interestingly, self-assembled nanofibers were observed in both peptides. For Azo-ffs_py (pH 4) at 20 μ M, the self-assembled product appeared at low concentration and was not homogeneous, comprising thin tubes with a diameter of 50 Å and ribbon-like structures with a long crossover repeat (Figure 5A). Upon imaging Azo-ffs_py (pH 4) at a higher concentration of \sim 100 μ M, we observed additional continuous 2D sheets in the image background (Figure S44). To gain a better understanding of the 2D sheets, we manually boxed 1,000 "background" particles without filaments. The power spectrum of these aligned background particles revealed features at 1/(4.9 Å), corresponding to cross- β packing, and 1/(11.5 Å), possibly indicating the spacing between adjacent parallel cross- β ribbons (Figure S44). On the other hand, no 2D sheets were found for Azo-ffsy at 20 or 100 μM concentration, and even at 20 µM concentration, Azo-ffsy exhibited very homogeneous, high-concentration nanofibers at a slightly smaller diameter of \sim 45 Å (Figure 5B).

To determine the helical symmetry of these nanofibers, we systematically tested all possible symmetries indexed from the averaged power spectrum (Figure S45A,B) through trial and error until recognizable densities for the peptide side chains

were seen. The final reconstructions of Azo-ffs_py (pH 4) and Azo-ffsy reached resolutions of 3.0 and 2.8 Å, respectively, as judged by the map:map FSC (Figure S45C,D). Both nanofibers exhibited C2 symmetry, but their packing was markedly different. Azo-ffs_py (pH 4) had a helical rise of 1.16 Å and a twist of 46.52 degrees, while Azo-ffsy had a helical rise of 1.31 Å and a twist of 63.37 degrees (Figure 5C,D). In both nanofibers, the "Azo" aromatic motifs were clustered inside the fiber, while the phosphorylated or dephosphorylated tyrosines were positioned near the surface. In the Azo-ffsy fiber, the tyrosine bends inward to make hydrophobic contacts with other residues, leaving the tube surface mostly to main chain residues and the side chain of serines. Such a conformation could not be maintained in Azo-ffs_py (pH 4), as the phosphate would be much more hydrophilic and repel from each other. In Azo-ffs_ny (pH 4), the phosphorylated tyrosines point outward, maintaining a conformation different from that of Azo-ffsy (Figure 5E,F). Structure determination reveals the presence of both tyrosine and carboxylate residues at the periphery of the nanofibers. This arrangement is similar to that observed in CsgA fibrils,²² which bind fibronectin.²³ Therefore, it is hypothesized that fibronectin can act as a binder and contribute to the alignment of the nanofibers within the bundles. This aligns with previous reports demonstrating that binder or associative interactions can induce fibril alignment, as seen in the generation of tactoids through actin filaments.²

Interestingly, Azo-ffsy nanofibers transitioned into a tube architecture different from that of Azo-ffs_py (pH 4). We asked the question whether there were any similarities between these packings and what residues needed to be reoriented for such an architectural shift, aside from the obvious $\pi - \pi$ stacking and beta-sheet hydrogen bonds between adjacent peptides. Strikingly, we could align two peptide pairs within those two nanofibers reasonably well at the backbone level (Figure S46). Aside from the previously mentioned tyrosine, the only significant difference was phenylalanine 2, pointing in different directions to accommodate the different tyrosine positions. Such phenomena, that similar interfaces found in dramatically different architectures, have previously been described as quasiequivalence²² or structural plasticity.²

This underscores the critical role of EISA in modulating the assembly behavior of fibronectin. Cryo-EM structure determination revealed that tyrosine folds back after dephosphorylation. Although the structure of Azo-ffs_ny was determined under acidic conditions (pH 4), the observed conformational change in the peptide is directly attributed to the loss of the phosphate group. These structural details provide an atomiclevel understanding of the EISA process, culminating in the pillar formation. We speculate that this enzyme-controlled mechanism represents a general strategy for generating higherorder protein structures, suggesting broader applications for EISA in controlling protein assemblies.

CONCLUSION

In summary, we present a cell-free approach for remodeling key ECM proteins, such as fibronectin and collagen, into mesoscale vertical pillars. While considerable reports have demonstrated the use of EISA of peptides for targeting cancer cells²⁶ or inhibiting tumor growth,²⁷ the exploration of cell-free application of EISA is rather limited. This method leverages the power of nonequilibrium self-assembly aspect of EISA at multiple scales.²⁸ Specifically, our work demonstrates that ALP triggers a multilevel morphological transformation. An Azo-

ffs_ny phosphopeptide initially exists as nanoparticles but, in the presence of ALP, undergoes a morphological shift to form nanofibers. In contrast to simple chemical reactions for chemical gardens, 29 enzyme-instructed self-assembly holds potential for precise control over nanoscale to microscale protein behavior. Crucially, when the self-assembly occurs under nonequilibrium conditions (i.e., during enzymatic reactions), it acts as a driving force for the morphogenesis of fibronectin into well-organized vertical peptide/protein composite pillars. These engineered structures can serve as templates to precisely modulate the organization of collagen (both type I and IV). Unlike traditional methods relying on achieving equilibrium states, 20,30 our method harnesses the power of nonequilibrium dynamics to build protein hierarchical nanostructures. This allows for unprecedented control over factors such as vertical fiber length, density, and morphology of the fibronectin structures. These parameters are primarily determined by reaction kinetics, which offer a high degree of tunability. Furthermore, cryo-EM analysis provides invaluable structural insights. We determined the structures for both Azo-ffs_py (pH 4) and the dephosphorylated Azo-ffsy nanofibers. This analysis revealed an inward bending of the C-terminal tyrosine in Azo-ffsy, highlighting structural changes induced by the enzymatic process.

Current results suggest that multiple factors, such as enzymatic activity, initial concentrations, nonequilibrium conditions, photoisomerization, morphological transformation of the peptide, surface interactions, temperature, and elastocapillary assembly, contribute to the observed vertical fibrils and indicate that enzymatic self-assembly is undoubtedly the key factor for this observation. Although the complete mechanism for the generation of vertical fibrils and pillars requires further studies, the critical factor is the nonequilibrium assembling process conferred by EISA, as no vertical pillar forms without the enzymatic reaction.

This work demonstrates cell-free manipulation of native proteins using nonequilibrium self-assembly techniques. Ultimately, these results may open avenues for future investigations into how these precisely engineered protein structures interact with living cells and influence their behavior. Understanding these interactions could have profound implications for regenerative medicine, tissue engineering, and the development of novel biomaterials.

ASSOCIATED CONTENT

Supporting Information

The Supporting Information is available free of charge at https://pubs.acs.org/doi/10.1021/jacs.4c06775.

Materials, instruments, and detailed experimental procedures, supporting schemes, figures, tables, discussions, and references of peptide synthesis, quantification of vertical bundles, experiment setup, LC-MS spectra of peptides, photochemical assays, enzymatic dephosphorylation, peptide self-assembly, fluorescence recovery after photobleaching, growth of vertical bundles, remodeling of collagen, cell morphogenesis, molecular optimization, theoretical analysis, and cryo-EM structural determination (PDF)

AUTHOR INFORMATION

Corresponding Authors

Fengbin Wang - Department of Biochemistry and Molecular Genetics, University of Alabama at Birmingham, Birmingham, Alabama 35294, United States; O'Neal Comprehensive Cancer Center University of Alabama at Birmingham, Birmingham, Alabama 35294, United States; orcid.org/0000-0003-1008-663X; Email: jerrywang@ uab.edu

Bing Xu - Department of Chemistry, Brandeis University, Waltham, Massachusetts 02453, United States; o orcid.org/ 0000-0002-4639-387X; Email: bxu@brandeis.edu

Jiaqi Guo - Department of Chemistry, Brandeis University, Waltham, Massachusetts 02453, United States; o orcid.org/ 0000-0002-0254-0401

Ayisha Zia - Department of Biochemistry and Molecular Genetics, University of Alabama at Birmingham, Birmingham, Alabama 35294, United States

Qianfeng Qiu - Department of Chemistry, Brandeis University, Waltham, Massachusetts 02453, United States Michael Norton - Department of Physics, Brandeis University,

Waltham, Massachusetts 02453, United States

Kangqiang Qiu - Department of Cancer Biology, Center for Chemical Imaging in Biomedicine, Advanced Cell Analysis Service Center, University of Cincinnati College of Medicine, Cincinnati, Ohio 45267, United States

Junichi Usuba - Department of Chemistry, Brandeis University, Waltham, Massachusetts 02453, United States

Zhiyu Liu - Department of Chemistry, Brandeis University, Waltham, Massachusetts 02453, United States

Meihui Yi – Department of Chemistry, Brandeis University, Waltham, Massachusetts 02453, United States; oorcid.org/ 0000-0002-1912-1043

Shane T. Rich-New - Department of Biochemistry and Molecular Genetics, University of Alabama at Birmingham, Birmingham, Alabama 35294, United States

Michael Hagan - Department of Physics, Brandeis University, Waltham, Massachusetts 02453, United States; oorcid.org/ 0000-0002-9211-2434

Seth Fraden - Department of Physics, Brandeis University, Waltham, Massachusetts 02453, United States

Grace D. Han – Department of Chemistry, Brandeis University, Waltham, Massachusetts 02453, United States

Jiajie Diao - Department of Cancer Biology, Center for Chemical Imaging in Biomedicine, Advanced Cell Analysis Service Center, University of Cincinnati College of Medicine, Cincinnati, Ohio 45267, United States; orcid.org/0000-0003-4288-3203

Complete contact information is available at: https://pubs.acs.org/10.1021/jacs.4c06775

Funding

This research was, in part, supported by the National Cancer Institute's National Cryo-EM Facility at the Frederick National Laboratory for Cancer Research under contract 75N91019D00024. Electron microscopy screening was carried out in the UAB Cryo-EM Facility, supported by the Institutional Research Core Program and O'Neal Comprehensive Cancer Center (NIH grant P30 CA013148), with additional funding from NIH grant S10 OD024978. The work in F.W. laboratory was supported by NIH grant GM138756. The work in B.X. laboratory was supported by NIH grant CA142746 and NSF MRSEC grant DMR-2011846. G.G.D.H. acknowledges the NSF CAREER award (DMR-2142887), Alfred P. Sloan Foundation (FG-2022-18328), and the Camille and Henry Dreyfus Foundation (TC-23-028).

The authors declare no competing financial interest.

ACKNOWLEDGMENTS

We are grateful to Dr. James Kizziah, Dr. Thomas Edwards, Dr. Tara Fox, Dr. Adam Wier, and Dr. Zhiqing Wang for assisting with the screening or data collection.

ABBREVIATIONS

ECM extracellular matrix ALP alkaline phosphatase rFN rhodamine-fibronectin **PBS** phosphate buffered saline absorbance at 323 nm $A_{323 \text{ nm}}$ Azo

azobenzene

ffD-phenylalanine-D-phenylalanine

(E)-stilbene SB ТВ diphenylethyne BB diphenylethane BP biphenyl Naph naphthalene

SPPS solid-phase peptide synthesis

LC-MS liquid chromatography-mass spectrometry **HPLC** high-performance liquid chromatography

 ΔH^{\ddagger} change in enthalpy ΔS^{\ddagger} change in entropy

CMCs critical micelle concentrations

CD circular dichroism

TEM transmission electron microscopy SIM structured illumination microscopy

PAP prostatic acid phosphatase **EISA** enzyme-instructed self-assembly.

REFERENCES

(1) (a) Klinge, S.; Woolford, J. L. Ribosome assembly coming into focus. Nat. Rev. Mol. Cell Biol. 2019, 20 (2), 116-131. (b) Doxsey, S. Re-evaluating centrosome function. Nat. Rev. Mol. Cell Biol. 2001, 2 (9), 688-698.

(2) Lu, A.; Magupalli, G. V.; Ruan, J.; Fitzgerald, K. A.; Wu, H.; Egelman, H. E. Unified Polymerization Mechanism for the Assembly of ASC-Dependent Inflammasomes. Cell 2014, 156 (6), 1193-1206. (3) Seybold, C.; Schiebel, E. Spindle pole bodies. Curr. Biol. 2013, 23 (19), R858-860.

(4) (a) Fontana, P.; Dong, Y.; Pi, X.; Tong, A. B.; Hecksel, C. W.; Wang, L.; Fu, T. M.; Bustamante, C.; Wu, H. Structure of cytoplasmic ring of nuclear pore complex by integrative cryo-EM and AlphaFold. Science 2022, 376 (6598), No. eabm9326. (b) Baquero, D. P.; Cvirkaite-Krupovic, V.; Hu, S. S.; Fields, J. L.; Liu, X.; Rensing, C.; Egelman, E. H.; Krupovic, M.; Wang, F. Extracellular cytochrome nanowires appear to be ubiquitous in prokaryotes. Cell 2023, 186 (13), 2853-2864.e8. (c) Steve, A.; Baumeister, W.; Johnson, L. N.; Perham, R. N. Molecular Biology of Assemblies and Machines; Garland Science, 2016. (d) Kreutzberger, M. A. B.; Wang, S.; Beltran, L. C.; Tuachi, A.; Zuo, X.; Egelman, E. H.; Conticello, V. P. Phenol-soluble modulins PSM α 3 and PSM β 2 form nanotubes that are cross- α amyloids. Proc. Natl. Acad. Sci. U. S. A 2022, 119 (20), No. e2121586119.

(5) Luo, Q.; Hou, C.; Bai, Y.; Wang, R.; Liu, J. Protein Assembly: Versatile Approaches to Construct Highly Ordered Nanostructures. Chem. Rev. 2016, 116 (22), 13571-13632.

- (6) Wu, H.; Fuxreiter, M. The Structure and Dynamics of Higher-Order Assemblies: Amyloids, Signalosomes, and Granules. *Cell* **2016**, 165 (5), 1055–1066.
- (7) Boekhoven, J.; Hendriksen, W. E.; Koper, G. J. M.; Eelkema, R.; Van Esch, J. H. Transient assembly of active materials fueled by a chemical reaction. *Science* **2015**, *349* (6252), 1075–1079.
- (8) Pokroy, B.; Kang, S. H.; Mahadevan, L.; Aizenberg, J. Self-organization of a mesoscale bristle into ordered, hierarchical helical assemblies. *Science* **2009**, 323 (5911), 237–240.
- (9) (a) Gu, Y.; Zhao, Y.; Ichikawa, M. Tektin makes a microtubule a "micropillar. *Cell* **2023**, *186* (13), 2725–2727. (b) Lin, J.; Nicastro, D. Asymmetric distribution and spatial switching of dynein activity generates ciliary motility. *Science* **2018**, *360* (6387), No. eaar1968.
- (10) (a) Baneyx, G.; Baugh, L.; Vogel, V. Fibronectin extension and unfolding within cell matrix fibrils controlled by cytoskeletal tension. *Proc. Natl. Acad. Sci. U. S. A.* **2002**, *99* (8), 5139–5143. (b) Little, W. C.; Smith, M. L.; Ebneter, U.; Vogel, V. Assay to mechanically tune and optically probe fibrillar fibronectin conformations from fully relaxed to breakage. *Matrix Biol.* **2008**, *27* (5), 451–461.
- (11) Sato, Y.; Nagatoshi, K.; Hamano, A.; Imamura, Y.; Huss, D.; Uchida, S.; Lansford, R. Basal filopodia and vascular mechanical stress organize fibronectin into pillars bridging the mesoderm-endoderm gap. *Development* **2017**, *144* (2), 281–291.
- (12) Liu, Z.; Guo, J.; Qiao, Y.; Xu, B. Enzyme-Instructed Intracellular Peptide Assemblies. Acc. Chem. Res. 2023, 56 (21), 3076–3088.
- (13) Feng, Z.; Wang, H.; Wang, F.; Oh, Y.; Berciu, C.; Cui, Q.; Egelman, E. H.; Xu, B. Artificial Intracellular Filaments. Cell Rep. Phys. Sci. 2020, 1 (7), 100085.
- (14) Guo, J.; Wang, F.; Huang, Y.; He, H.; Tan, W.; Yi, M.; Egelman, E. H.; Xu, B. Cell spheroid creation by transcytotic intercellular gelation. *Nat. Nanotechnol.* **2023**, *18* (9), 1094–1104.
- (15) Kubota, R.; Makuta, M.; Suzuki, R.; Ichikawa, M.; Tanaka, M.; Hamachi, I. Force generation by a propagating wave of supramolecular nanofibers. *Nat. Commun.* **2020**, *11* (1), 3541.
- (16) Majumder, P.; Singh, A.; Wang, Z.; Dutta, K.; Pahwa, R.; Liang, C.; Andrews, C.; Patel, N. L.; Shi, J.; de Val, N.; et al. Surface-fill hydrogel attenuates the oncogenic signature of complex anatomical surface cancer in a single application. *Nat. Nanotechnol.* **2021**, *16* (11), 1251–1259.
- (17) (a) Wu, X.; Zhai, J.; Li, Q.; Wang, H. The in vitro culture of mammalian embryos. *Nat. Methods* **2023**, 20 (12), 1855–1858. (b) Liang, G.; Ren, H.; Rao, J. A biocompatible condensation reaction for controlled assembly of nanostructures in living cells. *Nat. Chem.* **2010**, 2 (1), 54–60.
- (18) Reches, M.; Gazit, E. Casting Metal Nanowires Within Discrete Self-Assembled Peptide Nanotubes. *Science* **2003**, *300* (5619), 625–627.
- (19) (a) Nerger, B. A.; Brun, P.-T.; Nelson, C. M. Marangoni flows drive the alignment of fibrillar cell-laden hydrogels. *Sci. Adv.* **2020**, *6* (24), No. eaaz7748. (b) Te Brinke, E.; Groen, J.; Herrmann, A.; Heus, H. A.; Rivas, G.; Spruijt, E.; Huck, W. T. S. Dissipative adaptation in driven self-assembly leading to self-dividing fibrils. *Nat. Nanotechnol.* **2018**, *13* (9), 849–855.
- (20) Fu, H.; Huang, J.; van der Tol, J. J. B.; Su, L.; Wang, Y.; Dey, S.; Zijlstra, P.; Fytas, G.; Vantomme, G.; Dankers, P. Y. W.; et al. Supramolecular polymers form tactoids through liquid—liquid phase separation. *Nature* **2024**, *626* (8001), 1011—1018.
- (21) Liamas, E.; Kubiak-Ossowska, K.; Black, R. A.; Thomas, O. R. T.; Zhang, Z. J.; Mulheran, P. A. Adsorption of Fibronectin Fragment on Surfaces Using Fully Atomistic Molecular Dynamics Simulations. *Int. J. Mol. Sci.* **2018**, *19* (11), 3321.
- (22) Wang, F.; Cvirkaite-Krupovic, V.; Vos, M.; Beltran, L. C.; Kreutzberger, M. A. B.; Winter, J.-M.; Su, Z.; Liu, J.; Schouten, S.; Krupovic, M.; et al. Spindle-shaped archaeal viruses evolved from rod-shaped ancestors to package a larger genome. *Cell* **2022**, *185* (8), 1297–1307.e11.
- (23) Olsén, A.; Arnqvist, A.; Hammar, M.; Sukupolvi, S.; Normark, S. The RpoS sigma factor relieves H-NS-mediated transcriptional

- repression of csgA, the subunit gene of fibronectin-binding curli in *Escherichia coli. Mol. Microbiol.* **1993**, 7 (4), 523–536.
- (24) Weirich, K. L.; Banerjee, S.; Dasbiswas, K.; Witten, T. A.; Vaikuntanathan, S.; Gardel, M. L. Liquid behavior of cross-linked actin bundles. *Proc. Natl. Acad. Sci. U. S. A.* **2017**, *114* (9), 2131–2136.
- (25) Liu, J.; Eastep, G. N.; Cvirkaite-Krupovic, V.; Rich-New, S. T.; Kreutzberger, M. A. B.; Egelman, E. H.; Krupovic, M.; Wang, F. Two dramatically distinct archaeal type IV pili structures formed by the same pilin. *bioRxiv* **2023**.
- (26) (a) Tan, W.; Zhang, Q.; Quiñones-Frías, M. C.; Hsu, A. Y.; Zhang, Y.; Rodal, A.; Hong, P.; Luo, H. R.; Xu, B. Enzyme-Responsive Peptide Thioesters for Targeting Golgi Apparatus. J. Am. Chem. Soc. 2022, 144 (15), 6709-6713. (b) Yi, M.; Wang, F.; Tan, W.; Hsieh, J.-T.; Egelman, E. H.; Xu, B. Enzyme Responsive Rigid-Rod Aromatics Target "Undruggable" Phosphatases to Kill Cancer Cells in a Mimetic Bone Microenvironment. J. Am. Chem. Soc. 2022, 144 (29), 13055-13059. (c) Feng, Z.; Wang, H.; Wang, S.; Zhang, Q.; Zhang, X.; Rodal, A. A.; Xu, B. Enzymatic Assemblies Disrupt the Membrane and Target Endoplasmic Reticulum for Selective Cancer Cell Death. J. Am. Chem. Soc. 2018, 140 (30), 9566-9573. (d) Feng, Z.; Wang, H.; Chen, X.; Xu, B. Self-Assembling Ability Determines the Activity of Enzyme-Instructed Self-Assembly for Inhibiting Cancer Cells. J. Am. Chem. Soc. 2017, 139 (43), 15377-15384. (e) Feng, Z.; Wang, H.; Zhou, R.; Li, J.; Xu, B. Enzyme-Instructed Assembly and Disassembly Processes for Targeting Downregulation in Cancer Cells. J. Am. Chem. Soc. 2017, 139 (11), 3950-3953. (f) Liu, X.; Li, M.; Liu, J.; Song, Y.; Hu, B.; Wu, C.; Liu, A.-A.; Zhou, H.; Long, J.; Shi, L.; et al. In Situ Self-Sorting Peptide Assemblies in Living Cells for Simultaneous Organelle Targeting. J. Am. Chem. Soc. 2022, 144 (21), 9312-9323. (g) Cai, Y.; Shen, H.; Zhan, J.; Lin, M.; Dai, L.; Ren, C.; Shi, Y.; Liu, J.; Gao, J.; Yang, Z. Supramolecular "Trojan Horse" for Nuclear Delivery of Dual Anticancer Drugs. J. Am. Chem. Soc. 2017, 139 (8), 2876-2879. (h) Gao, G.; Jiang, Y.-W.; Zhan, W.; Liu, X.; Tang, R.; Sun, X.; Deng, Y.; Xu, L.; Liang, G. Trident Molecule with Nanobrush-Nanoparticle-Nanofiber Transition Property Spatially Suppresses Tumor Metastasis. J. Am. Chem. Soc. 2022, 144 (26), 11897-11910.
- (27) Feng, Z.; Han, X.; Wang, H.; Tang, T.; Xu, B. Enzyme-instructed peptide assemblies selectively inhibit bone tumors. *Chem* **2019**, 5 (9), 2442–2449.
- (28) (a) Epstein, I. R.; Xu, B. Reaction—diffusion processes at the nano- and microscales. *Nat. Nanotechnol.* **2016**, *11* (4), 312–319. (b) Whitesides, G. M.; Grzybowski, B. Self-Assembly at All Scales. *Science* **2002**, 295 (5564), 2418–2421.
- (29) Barge, L. M.; Cardoso, S. S. S.; Cartwright, J. H. E.; Cooper, G. J. T.; Cronin, L.; De Wit, A.; Doloboff, I. J.; Escribano, B.; Goldstein, R. E.; Haudin, F.; et al. From Chemical Gardens to Chemobrionics. *Chem. Rev.* **2015**, *115* (16), 8652–8703.
- (30) Whitesides, G. M.; Simanek, E. E.; Mathias, J. P.; Seto, C. T.; Chin, D.; Mammen, M.; Gordon, D. M. Noncovalent Synthesis: Using Physical-Organic Chemistry To Make Aggregates. *Acc. Chem. Res.* 1995, 28 (1), 37–44.